

NeVStereo: A NeRF-Driven NVS-Stereo Architecture for High-Fidelity 3D Tasks

Pengchen Chen^{*†}

University of Washington

pengcc@uw.edu

Yue Hu^{*†}

University of Southern California

yhu57782@usc.edu

Wenhao Li^{*‡}

CUHK-Shenzhen

wenhaoli1@link.cuhk.edu.cn

Nicole M Gunderson
University of Washington

nmgundo@uw.edu

Andrew Feng
USC Institute for Creative Technologies

feng@ict.usc.edu

Zhenglong Sun
CUHK-Shenzhen

sunzhenglong@cuhk.edu.cn

Peter Beerel
University of Southern California

pabeerel@usc.edu

Eric J Seibel
University of Washington

eseibel@uw.edu

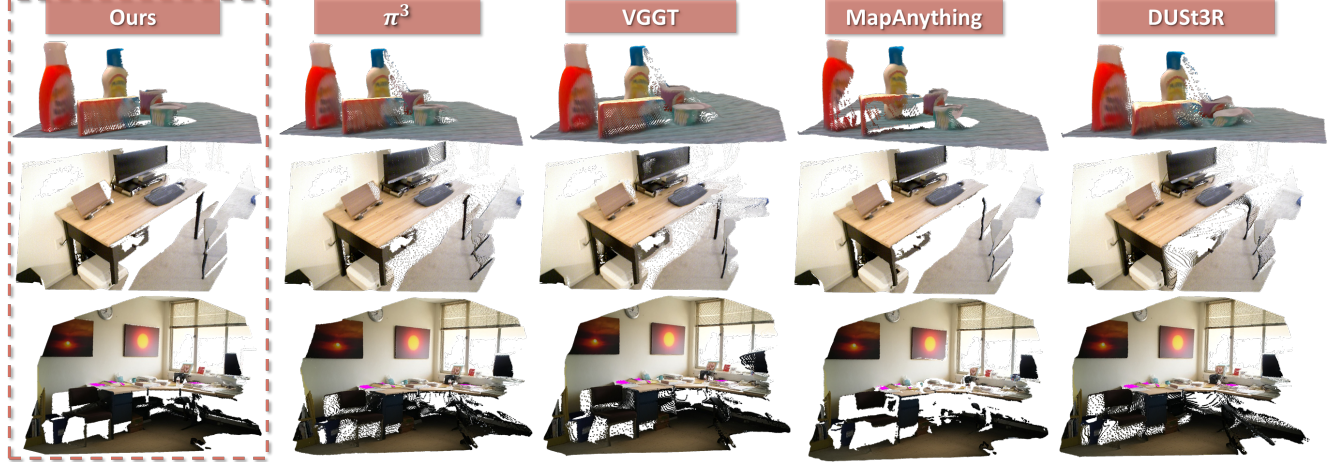


Figure 1. 3D reconstruction quality comparison. NeVStereo produces point clouds with more accurate geometry and significantly fewer floating artifacts than other methods.

Abstract

In modern dense 3D reconstruction, feed-forward systems (e.g., VGGT, π^3) focus on end-to-end matching and geometry prediction but do not explicitly output the novel view synthesis (NVS). Neural rendering-based approaches offer high-fidelity NVS and detailed geometry from posed images, yet they typically assume fixed camera poses and can be sensitive to pose errors. As a result, it remains non-trivial to obtain a single framework that can offer accurate poses, reliable depth, high-quality rendering, and accurate 3D surfaces from casually captured views. **We present NeVStereo,**

a NeRF-driven NVS-stereo architecture that aims to jointly deliver camera poses, multi-view depth, novel view synthesis, and surface reconstruction from multi-view RGB-only inputs. NeVStereo combines NeRF-based NVS for stereo-friendly renderings, confidence-guided multi-view depth estimation, NeRF-coupled bundle adjustment for pose refinement, and an iterative refinement stage that updates both depth and the radiance field to improve geometric consistency. This design mitigated the common NeRF-based issues such as surface stacking, artifacts, and pose-depth coupling. Across indoor, outdoor, tabletop, and aerial benchmarks, our experiments indicate that NeVStereo achieves consistently strong zero-shot performance, with up to **36% lower depth error, 10.4% improved pose accuracy, 4.5% higher NVS fidelity, and state-of-the-**

^{*}Co-first authors, equal contribution.

[†]Primary contributors to the main methods and evaluation.

[‡]Contributed to preliminary study.

art mesh quality (**F1 91.93%, Chamfer 4.35 mm**) compared to existing prestigious methods.

1. Introduction

Modern 3D vision increasingly demands reconstruction systems that deliver accurate geometry, reliable camera poses, and photorealistic novel view synthesis (NVS) from casually captured multi-view images [4, 19, 24, 41], for applications such as robotics, AR/VR [35], cultural heritage digitization [8, 43], and image-guided surgery [7, 49]. This raises a central question: can we design a reconstruction paradigm that simultaneously provides high-accuracy 3D geometry, robust pose estimation, and high-quality NVS across diverse scene scales, baselines, and capture conditions?

Recent progress toward this goal has largely followed two separate lines. Feed-forward 3D systems such as MaSt3R [20], VGGT [39], and π^3 [42] focus on end-to-end matching, geometry reconstruction, and pose estimation from dense multi-view images, offering strong geometric priors but no explicit NVS module. Neural rendering-based methods (e.g., 2DGS [14], Neuralangelo [22], NeuS [40], SUGAR [11]) instead optimize a neural scene representation from posed images for high-quality NVS and 3D reconstruction, yet typically keep camera poses fixed and remain sensitive to pose errors.

To bridge the missing components of these two lines, we consider an alternative paradigm, *NVS-stereo*: use NVS to render high-fidelity stereo pairs, then apply a powerful stereo depth estimator to the synthesized pairs, and finally feed the resulting depth back to refine poses, NVS quality, and a fused 3D mesh. This idea is not purely conceptual: prior work has already combined 3D Gaussian Splatting (3DGS) with NVS-stereo for depth estimation and reconstruction [30, 45], but with poses fixed to the original SfM solution. To understand whether this limitation stems from NVS-stereo itself or from the underlying representation, we conduct a systematic comparison between 3DGS- and NeRF-based NVS-stereo pipelines. Our analysis shows that 3DGS-based NVS-stereo quickly saturates at the SfM accuracy ceiling, whereas NeRF-based NVS-stereo can surpass this ceiling by producing smoother, more accurate, and more multi-view-consistent depth.

Building on these insights, we propose **NeVstereo**: a complete NeRF-based NVS-Stereo framework that integrates novel view synthesis, stereo depth estimation, pose optimization, depth fusion, and iterative refinement (Fig. 3). It effectively addresses all the aforementioned challenges. Our method achieves state-of-the-art performance in camera pose estimation, multi-view depth estimation, novel view synthesis, and surface reconstruction, and surpasses most prestigious existing methods. Specifically, our

contributions are as follows:

- **NeRF-based high-accuracy NVS-Stereo reconstruction.** We introduce the first NeRF-based NVS-stereo architecture that achieves high-accuracy pose, depth novel view synthesis, and 3D reconstruction at the same time, through our designed pose optimization and NeRF iterative pipeline. By using refined depths and poses to focus sampling on true surfaces and filtering NeRF artifacts with confidence-aware stereo cues, our method yields more geometrically consistent NVS, supports larger baselines, and delivers highly accurate depth and 3D geometry.
- **Systematic study of NVS-Stereo reconstruction.** We provide the statistical analysis of NVS-Stereo pipelines, revealing core failure modes and, through controlled 3DGS-vs.-NeRF comparisons, demonstrating that 3DGS-based NVS-Stereo saturates at the SfM ceiling and when NeRF can surpass it.
- **Strong empirical performance and generalization.** Across indoor/outdoor, tabletop and UAV benchmarks, our architecture outperforms SOTA baselines, achieving up to 36% lower **depth** error, 10.4% better **pose** accuracy (RTE 0.0215 vs. 0.0240), 4.5% higher **NVS render** PSNR, and best-in-class **mesh** quality (F1 91.93% vs. 89.30%; Chamfer 4.35 mm vs. 4.74 mm).

2. Related Works

Novel View Synthesis: Synthesizing high-quality stereo view pairs from known viewpoints is the cornerstone of our pipeline. Among NeRF-based NVS methods, ZipNeRF [2] remains state-of-the-art across diverse datasets, producing anti-aliased, view-consistent renderings with stable geometry that are well suited for downstream stereo. It combines anti-aliased volumetric rendering, multi-scale supervision, and proposal-driven sampling with a coarse-to-fine training schedule, yielding sharper textures, fewer floaters, and improved handling of thin and specular structures.

Stereo depth estimation: Stereo has evolved from attention/transformer and deformable-CNN pipelines (e.g., MatchStereo [16], DEFOM-Stereo [15]) to large, pre-trained foundation models such as FoundationStereo [44]. While MatchStereo and DEFOM-Stereo offer strong correspondence filtering within their training domains, they generally require task- or dataset-specific tuning under photometric shifts or weak texture. In contrast, FoundationStereo, trained at scale with monocular priors, achieves strong zero-shot generalization and remains robust under low texture, specularities, illumination changes, and the syn-to-real gap introduced by NVS rendering.

RGB-D optimization: Classical geometric RGB-D SLAM systems such as ORB-SLAM [5, 25], BAD-SLAM [32], and DROID-SLAM [34] jointly estimate poses and structure from photometric and geometric residuals via

robust data association and bundle adjustment. Neural rendering-based SLAM instead optimizes camera trajectories against a learned scene representation: GS-SLAM [46], SplatTAM [17] and SplatMAP [13] use 3D Gaussian Splatting for efficient mapping, while NeRF-SLAM [29] maintains a volumetric radiance field that provides dense photometric gradients. In this work, we combine these two paradigms by optimizing camera poses under geometric constraints while simultaneously refining rendering quality through neural rendering supervision (Sec. 4).

3. Preliminary Study and Challenges

To compare the NeRF backbone and the 3DGS backbone for NVS-stereo, we evaluate both on the NVIDIA-HOPE[36] and Redwood RGB-D[26] datasets. We first conduct a cross-dataset analysis using Redwood RGB-D and NVIDIA HOPE to examine how differences in SfM quality affect overall NVS-stereo performance. We then perform an in-depth study within NVIDIA HOPE to analyze how the precision of SfM initialization influences NeRF and 3DGS-based NVS-stereo results.

We use Nerfacto (without pose optimization) and vanilla 3DGS as backbones, both initialized from COLMAP. Depth maps are obtained by rendering training views as left images, synthesizing novel right views with a fixed baseline, and running FoundationStereo for stereo estimation. Hyperparameters are tuned on 20% of scenes and fixed for the remaining 80%. Training stops when $\text{PSNR} \geq 35$. As shown in Tab. 1, we found that the NeRF-based NVS-Stereo performance outperforms the COLMAP and 3DGS-based methods on both absrel and $\delta < 5\%$, meanwhile, the 3DGS-based NVS-Stereo didn't surpass COLMAP's performance.

Method	NVIDIA-HOPE		Redwood RGB-D	
	absrel \downarrow	$\delta < 5\% \uparrow$	absrel \downarrow ($\Delta\%$)	$\delta < 5\% \uparrow$ ($\Delta\%$)
COLMAP	0.019	93.80%	0.048 (+152.4%)	79.94% (-14.8%)
3DGS based	0.023	94.32%	0.048 (+110.9%)	82.21% (-12.8%)
Nerfacto based	0.018	95.47%	0.023 (+33.7%)	91.08% (-4.6%)

Table 1. Depth accuracy on NVIDIA-HOPE and Redwood RGB-D. NeRF-based NVS-Stereo performs best on both metrics, while 3DGS-based NVS-Stereo does not surpass COLMAP and degrades more under weakened SfM initialization.

When SfM quality degrades across datasets (Tab. 1), 3DGS accuracy drops nearly as much as COLMAP, while NeRF remains more stable. To investigate this difference, we examine frames with the largest performance gap in Fig. 2. While the left (training) views appear nearly identical, the right (novel) views reveal that 3DGS produces sharper, structured artifacts that disrupt stereo correspondence, whereas NeRF's low-frequency artifacts are less harmful to matching.

On NVIDIA-HOPE, we relate pose error to the fraction of pixels with $\delta < 5\%$, shown in Tab. 2. Within $\pm 1\sigma$ of

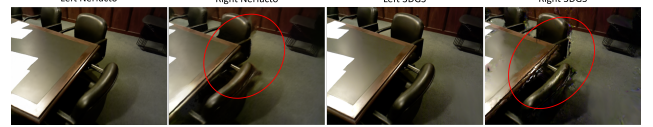


Figure 2. Artifact comparison under degraded SfM initialization. While input-view renderings look similar, the novel views show that 3DGS produces sharper, structured artifacts than NeRF. These artifacts disrupt stereo correspondence and explain the larger accuracy drop of 3DGS-based NVS-stereo.

Method	ATE		RTE		RRE	
	Pearson	Spearman	Pearson	Spearman	Pearson	Spearman
3DGS ^N	-0.071	-0.050	-0.011	-0.038	-0.025	-0.043
Nerfacto ^N	-0.059	-0.049	-0.026	-0.034	-0.044	-0.062
3DGS ^O	-0.463	-0.461	-0.170	-0.175	-0.283	-0.294
Nerfacto ^O	-0.238	-0.267	-0.215	-0.143	-0.169	-0.089

Table 2. Correlation between depth accuracy ($\delta < 5\%$ fraction) and pose error on NVIDIA-HOPE. Superscripts mark pose-error regimes: ^N within 1σ (normal), ^O greater than 1σ (outlier). RTE = RPE_{trans} ($\delta = 1$); RRE = RPE_{rot} ($\delta = 1$).

the pose-error distribution, neither NeRF-based nor 3DGS-based NVS-Stereo shows a significant correlation, meaning that the depth gap is not pose-driven in the typical regime, in this portion, both NeRF and 3DGS performs a good rendering quality, depth estimation algorithm dominants the performance. However, beyond 1σ , correlations increase for both. NeRF-based NVS-Stereo shows only weak dependence (Pearson $r \approx -0.24$ across ATE/RRE/RTE), whereas 3DGS-based shows moderate dependence ($r \approx -0.46$ in ATE and $r \approx -0.3$ in RRE), consistently stronger than NeRF-based. More analysis diagrams are shown in **the supplementary material**.

Based on these experiments, we offer the following explanation: 3DGS, as a semi-dense representation initialized from SfM points, inherits both the strengths and weaknesses of the underlying reconstruction. It effectively behaves like a dense extension of COLMAP's PatchMatch stereo, with performance tightly coupled to SfM quality. In under-constrained regions, its semi-dense nature tends to produce high-frequency, blocky artifacts with sharp discontinuities, which corrupt the cost volume and severely disrupt stereo correspondence. By contrast, NeRF learns a continuous, dense field with smoothly varying texture and geometry across neighboring rays, yielding a cleaner cost volume with sharper dominant peaks and more stable stereo matching. NeRF depends only on camera poses rather than SfM point clouds, and is therefore less rigidly tied to SfM's global geometry. In regions with pose bias, it tends to favor local photometric consistency over strict global accuracy, preserving high local fidelity at the cost of slight global misalignment. Its artifacts are predominantly low-frequency, fog-like structures instead of sharp discontinuities, which

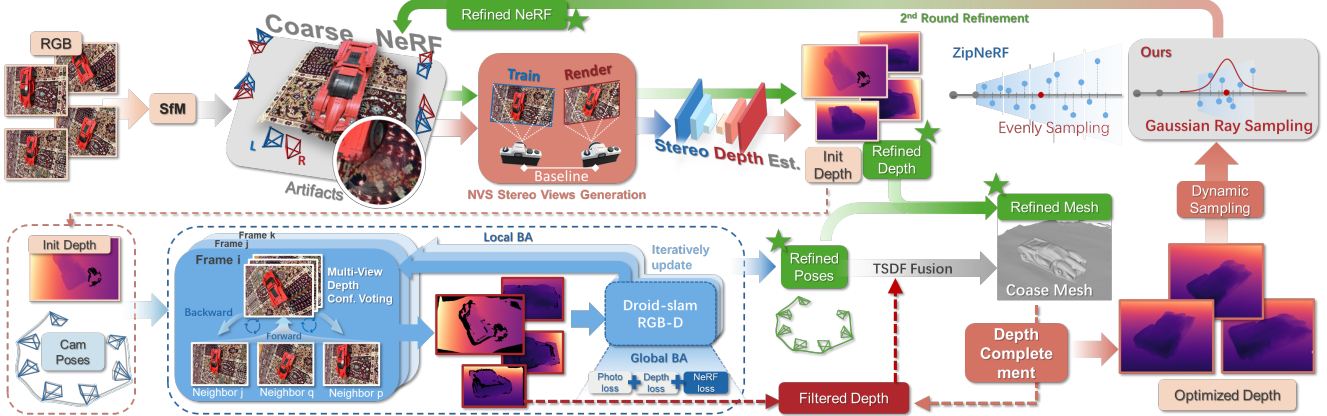


Figure 3. Architecture overview. Multi-view RGB inputs yield an initial SfM reconstruction and a coarse NeRF, which renders stereo pairs for depth estimation. The resulting depths are refined using our modified DROID-SLAM with multi-view depth voting and a NeRF-guided reprojection loss, followed by TSDF fusion and depth completion. The optimized depths then supervise a second-round NeRF refinement using our depth-guided Gaussian ray sampling for improved geometric accuracy. ★ Green highlights denote our outputs.

are generally less harmful to modern stereo estimators and thus more favorable for depth estimation.

Therefore, within an NVS-stereo pipeline, NeRF can provide better single-frame depth accuracy than 3DGs. However, this does not make NeRF an overall better backbone for 3D tasks: **it introduces several stringent challenges due to its lack of an explicit multi-view consistency constraint** that constrains the practical deployment of a NeRF-based NVS-Stereo pipeline:

(1) Inconsistent point cloud stacking: Point-cloud stacks from NeRF-based NVS-stereo can exhibit noticeable inconsistencies (Fig. 4A). This due to the NeRF relies only on SfM poses without explicit geometric regularization, so NVS-stereo depths from different viewpoints may not coincide on the same surface points. Pose-refinement methods such as BARF [23] and CamP [27] can improve photometric quality but mainly introduce small pose corrections and do not fully resolve these geometric discrepancies, suggesting that NeRF-based NVS-stereo needs additional pose optimization and RGB-D fusion. **(2) Artifacts:** NeRF-generated views may contain floating or layered artifacts (Fig. 4B/C) that are not easily removed by simple filtering. Such artifacts introduce instability into depth supervision and downstream pose optimization. Applying conventional RGB-D fusion directly on unfiltered depth maps can therefore lead to under-converged or noisy reconstructions (Fig. 4D). **(3) Rendering-geometry trade-offs:** The quality of NeRF rendering directly impacts stereo depth. Depth-supervised iterative refinement has been explored [7], but without joint pose optimization its gains can be limited in the presence of issues (1) and (2). Moreover, recent studies [12, 28, 37] indicate that naively adding depth supervision may even degrade rendering quality, as depth and RGB losses can compete during optimization, highlighting

the need for more carefully coupled objectives.



Figure 4. Stereo-depth projection without explicit multi-view constraints produces non-coincident, layered surfaces stacking. Even with accurate per-pixel depths, NeRF’s geometry can drift/ghost across views, breaking cross-view consistency. This **cannot be solved** by pose-optimized NeRF (BARF or CamP).

4. Method

In our method, we adopt ZipNeRF as the backbone for NVS-stereo. ZipNeRF provides strong anti-aliasing and view-consistency properties, which ensure that the synthesized stereo pairs yield reliable initial depths for downstream optimization. To address the challenges in Sec. 3, we propose a Multi-View Confidence-Guided Self-Supervised RGB-D Optimization (Mv-CG) framework with iterative depth-confidence voting and dynamic supervision updates. Our pose optimization framework is inherited from DROID-SLAM, but unlike the original DROID-SLAM, which treats depth as fixed, our method closes an EM-like (Expectation–Maximization) loop: after each bundle adjustment, we recompute cleaner, multi-view-consistent su-

pervisory depth using updated poses and feed it back to the next BA round.

Multi-View Depth Confidence Voting: Let there I_{ref} be a reference frame with depth D_{ref} , intrinsics $K = [f_x, f_y, c_x, c_y]$, and extrinsics (R_{ref}, t_{ref}) . For N neighboring frames $\{I_i, D_i, (R_i, t_i)\}_{i=1}^N$, we evaluate bidirectional consistency for each pixel (u, v) .

Forward projection ($ref \rightarrow src_i$): A 3D point is unprojected from (u, v) using $d_{ref} = D_{ref}(u, v)$:

$$\mathbf{p}_{cam}^{ref} = \begin{bmatrix} (u - c_x) d_{ref} / f_x \\ (v - c_y) d_{ref} / f_y \\ d_{ref} \end{bmatrix}, \quad \mathbf{p}_{world} = R_{ref}^\top (\mathbf{p}_{cam}^{ref} - t_{ref}). \quad (1)$$

It is then transformed to camera i and projected:

$$\mathbf{p}_{cam}^{src_i} = R_i \mathbf{p}_{world} + t_i, \quad \begin{bmatrix} u_{src} \\ v_{src} \end{bmatrix} = \begin{bmatrix} f_x p_x^{src_i} / p_z^{src_i} + c_x \\ f_y p_y^{src_i} / p_z^{src_i} + c_y \end{bmatrix}. \quad (2)$$

Let d_{src}^{interp} be bilinear interpolation of D_i at (u_{src}, v_{src}) . Forward depth consistency holds if

$$\frac{|d_{src}^{interp} - p_z^{src_i}|}{p_z^{src_i}} < \tau_{depth}. \quad (3)$$

Backward projection ($src_i \rightarrow ref$): The interpolated depth is back-projected and reprojected to the reference frame. The reprojection error e_{reproj} and depth ratio must satisfy

$$e_{reproj} < \tau_{reproj} \quad \text{and} \quad \frac{|p_z^{ref, back} - d_{ref}|}{d_{ref}} < \tau_{depth}. \quad (4)$$

Bidirectional consistency is defined as

$$C_i(u, v) = \mathbf{1}\{\text{Eqs. (3), (4) hold}\}. \quad (5)$$

The total vote and confidence map are then

$$V(u, v) = \sum_{i=1}^N C_i(u, v), \quad \text{Confidence}(u, v) = \frac{V(u, v)}{N}, \quad (6)$$

and pixels supported by at least m_{vote} views are retained:

$$M(u, v) = \begin{cases} 1, & V(u, v) \geq m_{vote}, \\ 0, & \text{otherwise.} \end{cases} \quad D_{\text{filtered}} = M \odot D_{ref}. \quad (7)$$

We initialize camera extrinsics with existing COLMAP results and perform an initial round of multi-view voting to obtain a coarse confidence map and filtered depth supervision, yielding a stable geometric prior that removes large artifacts before refinement. The voting loss is shown in Eq. (8), minimizing L_{vote} maximizes the per-image ratio of pixels that pass the multi-view consistency threshold, thereby encouraging geometric consistency of the supervisory depth; here Ω_r denotes the set of valid pixels

in the reference image r (with $|\Omega_r|$ its size), $V_r(u, v)$ is the multi-view vote count at pixel (u, v) , m_{vote} is the pass threshold, τ_m controls the softness of the decision, and $s(x) = 1/(1 + e^{-x})$ is the logistic function.

$$L_{vote} = 1 - \frac{1}{|\Omega_r|} \sum_{(u, v) \in \Omega_r} s\left(\frac{V_r(u, v) - m_{vote}}{\tau_m}\right), \quad (8)$$

Confidence-Weighted RGB-D Optimization: Within each local DROID-SLAM window, we jointly optimize camera poses $\{\mathbf{T}_i\}$ and dense predicted depths $\{D_i^{pred}\}$ by minimizing

$$E = E_{\text{photo}} + E_{\text{depth}}, \quad (9)$$

where E_{photo} is the standard photometric term and the RGB-D term is

$$E_{\text{depth}} = \underbrace{\sum_{u, v} w(u, v) \rho\left(D^{pred}(u, v) - D^{obs}(u, v)\right)^2}_{\text{RGB-D term (optimizes poses)}} + \lambda_{vote} L_{vote}. \quad (10)$$

Here D^{obs} is the current supervisory depth map (initialized from stereo using COLMAP poses), $\rho(\cdot)$ is a robust loss, and the weight

$$w(u, v) = \text{Confidence}(u, v) \cdot w_{\text{robust}} \quad (11)$$

combines multi-view geometric confidence with robust iteratively reweighted least squares weighting. The total depth loss combines the confidence-weighted RGB-D supervision with the voting loss L_{vote} , which encourages a higher proportion of pixels passing multi-view consistency.

Iterative Supervision Refinement. After each local BA, we recompute multi-view consistency using the updated poses to obtain a refined stereo depth \tilde{D}^{st} and confidence mask M . The supervisory depth is then updated via confidence-guided fusion:

$$D_{t+1}^{obs}(u, v) = \begin{cases} (1 - \beta) D_t^{obs}(u, v) + \beta \tilde{D}_t^{st}(u, v), & \text{if } M_t(u, v) = 1, \\ D_t^{obs}(u, v), & \text{otherwise,} \end{cases} \quad (12)$$

where β controls the update smoothness. To realize a coarse-to-fine schedule, we gradually anneal the consistency thresholds over iterations:

$$\tau_{\text{depth}}^{(t+1)} = \alpha \tau_{\text{depth}}^{(t)}, \quad \tau_{\text{reproj}}^{(t+1)} = \alpha \tau_{\text{reproj}}^{(t)}. \quad (13)$$

As the poses converge, thresholds are gradually tightened, and the supervision update relies increasingly on the most reliable high-confidence pixels.

Global BA with NeRF Coupling: Previous work shows that geometric RGB-D methods underperform COLMAP on NVS metrics [1], while neural rendering-based SLAM systems incorporating NVS loss match or surpass COLMAP by directly reducing rotation errors [29, 50].



Figure 5. Pose optimization effectively eliminates the erroneous surface stacking shown in Fig. 4. By refining camera poses under our proposed mechanism, the projected depths from different views converge onto a coherent surface, yielding clean and well-aligned geometry across all viewpoints.

Concretely, on top of the global photo and depth optimization objective, we attach a 1/8-scale NeRF branch based on Nerfacto and adopt a hash-grid-aware coarse-to-fine schedule: Training first focuses on low-resolution hash levels with coarse proposal-guided sampling, then transitions to higher resolution and finer sampling to stabilize joint pose–radiance optimization.

Let $\mathcal{S}_{1/8}$ denote 1/8 spatial downsampling and \mathcal{R}_θ the NeRF renderer parameterized by θ . For each active frame i , we render $\hat{I}_i^{(1/8)} = \mathcal{R}_\theta(\mathbf{T}_i, K/8)$ and define the NeRF photometric loss (no confidence weighting) as

$$E_{\text{nerf}} = \sum_{i \in \mathcal{A}} \sum_{\mathbf{x} \in \Omega^{(1/8)}} \rho \left(\left\| \hat{I}_i^{(1/8)}(\mathbf{x}) - \mathcal{S}_{1/8}(I_i)(\mathbf{x}) \right\|_1 \right). \quad (14)$$

The overall global objective becomes

$$E_{\text{global}} = E_{\text{photo}} + E_{\text{depth}} + \lambda_{\text{nerf}} E_{\text{nerf}}. \quad (15)$$

Within \mathcal{R}_θ , the multi-resolution hash grid and proposal sampling naturally realize a coarse-to-fine behavior without per-pixel confidence reweighting, allowing long-range (loop) constraints, dense RGB-D geometry, and low-resolution NeRF photometrics to jointly regularize the same pose set $\{\mathbf{T}_i\}$ and prevent depth-induced pose degradation. With our proposed Mv-CG pose optimization mechanism, the stacking artifacts are largely eliminated. The produced well-aligned geometry illustrated in Fig. 5.

Depth Fusion and NeRF Iteration: After the above optimization stages, we obtain refined camera poses together with a filtered stereo depth map. To fill holes and suppress flickering artifacts in stereo depth estimation [3], we first perform TSDF fusion using the optimized poses and filtered depths. We then render depth maps from the fused TSDF mesh, align them with the filtered stereo depth, and use the TSDF depth to complete missing regions (see supplementary material for details). The resulting artifact-reduced, hole-filled depth combined with the refined poses is then used to address the rendering-quality limitation discussed in Sec. 3. We adopt a depth-guided iterative strategy in the spirit of [7] to further improve ZipNeRF [2]. Unlike [7], we do not impose a direct depth loss, which may compete with the RGB objective. Instead, we guide ZipNeRF’s sam-

pling using the optimized poses and completed depth, biasing samples along each ray toward the stereo-estimated surface geometry. For each pixel, we follow the standard NeRF convention and parameterize a camera ray as

$$\mathbf{r}(t) = \mathbf{o} + t \mathbf{d}, \quad t \in [t_n, t_f], \quad (16)$$

where \mathbf{o} is the camera origin, \mathbf{d} is the unit viewing direction, and t denotes the depth along the ray. The completed depth \hat{d} simply specifies a preferred location along this ray for geometry-guided sampling.

$$p(t) = \frac{1}{Z} \exp \left(-\frac{(t - \hat{d})^2}{2\sigma_d^2} \right), \quad Z = \int_{t_n}^{t_f} \exp \left(-\frac{(s - \hat{d})^2}{2\sigma_d^2} \right) ds, \quad (17)$$

and draw sampling points using the inverse transform of the truncated Gaussian:

$$t_j = \hat{d} + \sigma_d \Phi^{-1}(\Phi_a + u_j(\Phi_b - \Phi_a)), \quad u_j \sim \mathcal{U}(0, 1), \quad (18)$$

where $\Phi(\cdot)$ denotes the standard normal CDF and $\Phi_a = \Phi\left(\frac{t_n - \hat{d}}{\sigma_d}\right)$, $\Phi_b = \Phi\left(\frac{t_f - \hat{d}}{\sigma_d}\right)$. This strategy concentrates sampling density around the estimated surface while keeping the ray sampling continuous and fully differentiable, enabling ZipNeRF to improve rendering quality and geometry without suffering from depth–RGB loss competition.

Outputs: After the NeRF iteration stage, we obtain a refined ZipNeRF model and use it to synthesize stereo pairs with a substantially larger baseline than the initial NVS-stereo setup. The increased stereo baseline yields larger disparity and therefore leads to more accurate depth estimates. Moreover, the refined ZipNeRF concentrates its sampling cones tightly around the true surface, leading to an explicit form of multi-view geometric consistency. As a result, the NVS-stereo depth no longer exhibits point-cloud stacking inconsistencies and can be directly fused into a mesh via TSDF fusion. An overview of the full pipeline is provided in Fig. 3. Our system produces four main outputs: optimized camera poses, multi-view depth, the iteratively refined ZipNeRF, and the final reconstructed mesh. These outputs are highlighted with **green stars** in Fig. 3, and their quantitative performance is evaluated in the subsequent experiments.

5. Experiments

We evaluate our method across four core tasks: camera pose estimation Sec. 5.1, multi-view depth estimation Sec. 5.2, novel view synthesis 5.3 and surface reconstruction Sec. 5.4. Across all tasks, our method consistently achieves state-of-the-art performance compared with existing approaches. To further verify the effectiveness and robustness of our design, we conduct a series of ablation studies, including analyses of the impact of Mv-CG mechanism

and NeRF coupling mechanism. Since earlier datasets were limited by video quality or ground truth accuracy, we adopt datasets collected within the last three years for our experiments. All ground-truth data are obtained either from high-accuracy sensors or synthetic sources with verified sub-millimeter accuracy. All the experiments are running on an H100 server; the setup details are shown in the **Supplementary Material**

5.1. Camera Pose Estimation

In this section, we feed all images into each feed-forward model in a single batch to obtain full trajectories for evaluation, as reported in Tab. 3. Under dense input, optimization-based methods such as VGGsFm [38] and COLMAP [38] remain highly competitive, particularly in rotation error. On small-scale, densely sampled scenes like Mobilebrick, feed-forward models show somewhat weaker performance relative to the optimization-based baselines. Our method outperforms both families across all metrics and surpasses the initial COLMAP poses, indicating that the proposed multi-view confidence-guided optimization and NeRF coupling can escape SfM local minima and further refine camera trajectories. We show the single frame’s trajectory and pose accuracy comparison in Fig. 7

Method	NVIDIA-HOPE(m)			Mobilebrick(mm)		
	ATE ↓	RTE ↓	RRE° ↓	ATE ↓	RTE ↓	RRE° ↓
COLMAP [31]	0.1461	0.0257	1.65	1.852	0.967	0.0671
VGGsFm [38]	0.1460	0.0246	1.67	2.064	0.955	0.0660
VGGT [39]	0.1261	0.0240	3.21	8.318	5.263	0.4389
MapAnything [18]	0.1491	0.0271	2.02	21.11	14.748	1.7432
π^3 [42]	0.1458	0.0352	1.62	6.311	4.452	0.3621
Ours	0.1450	0.0215	1.61	1.749	0.933	0.0649

Table 3. Average camera pose error across methods and datasets. Best, second-best, and third-best results are highlighted.

5.2. Multi-View Depth Estimation

For the multi-view depth estimation task, we evaluate a range of state-of-the-art methods on four domains: synthetic (Replica [33]), indoor (ScanNet++ [47]), tabletop (NVIDIA-HOPE [36]), and aerial (WildUAV [9]), to assess generalization across scene scale, texture, and sensing conditions. Our experimental set includes the full Replica and NVIDIA-HOPE datasets and a ScanNet++ NVS-DSLR validation subset. Feed-forward methods are configured with a 3D reconstruction batch size of 25 (their empirically optimal setting), and we perform scale-invariant evaluation by applying only per-frame scale alignment. As reported in Tab. 4, our method achieves the best absrel and $\delta < 5\%$ scores across all benchmarks. Notably, on ScanNet++, we outperform DUST3R [41], MonST3R [48], VGGT [39], and π^3 [42], even though ScanNet++ is part of their training corpus. Point cloud visualizations in Fig. 1 further indicate that our method tends to produce cleaner, more accurate geometry, whereas π^3 [42] and VGGT [39] often exhibit floating

points and distortions, and MapAnything [18] shows more holes and warping.

5.3. Novel View Synthesis

We evaluate our method on the task of novel view synthesis using the same ScanNet++ validation subset. Our method in this section is the iteratively refined ZipNeRF, while baseline methods include vanilla 3DGS, Nerfacto, and vanilla ZipNeRF trained with COLMAP poses. Our method achieves the highest PSNR and SSIM and the lowest LPIPS, showing clear advantages in both photometric fidelity and perceptual quality compared with all baselines. Fig. 8 provides a visual comparison, demonstrating that our results are more photorealistic with noticeable improvements in color accuracy and fine details compared to the initial ZipNeRF.

5.4. Surface Reconstruction

We evaluate on Mobilebrick [21] by fusing our final depths and optimized poses. As summarized in Tab. 5, our method achieves the best overall results. Qualitative results are shown in Fig. 6. As illustrated, our reconstructed meshes tend to be cleaner and more complete than those from traditional MVS pipelines (COLMAP with ground-truth poses and MVSFormer), with fewer artifacts and clearer structures. Compared with GS2Mesh, our method often recovers finer geometric details and exhibits more consistent surfaces.

5.5. Ablation Study

In this section, we investigate the effects of the confidence voting mechanism and NeRF coupling on both pose estimation and rendering quality. We perform a step-by-step analysis on the Mobilebrick dataset and additionally evaluate NeRF quality by holding out 5% of camera views as a test set and training Nerfacto (without pose optimization) for 25K iterations. The results are summarized in Tab. 6. Directly optimizing poses with DROID-RGBD and unfiltered depth leads to degraded pose accuracy relative to COLMAP and also lower NeRF scores, indicating that naively applying RGB-D optimization can introduce both geometric drift and rendering instability. Introducing the Mv-CG mechanism improves all pose metrics and brings them close to COLMAP; however, the NeRF metrics slightly decrease, suggesting that more consistent local geometry does not necessarily translate into better global radiance-field reconstruction when pose and rendering remain decoupled. We also evaluate 3DGS-based NVS-stereo depth under the same Mv-CG framework and observe only marginal gains in both pose and NeRF metrics. A possible explanation is that 3DGS inherits COLMAP’s systematic depth biases, which Mv-CG cannot fully remove, limiting its corrective effect. In contrast, using NeRF-derived NVS-stereo depth

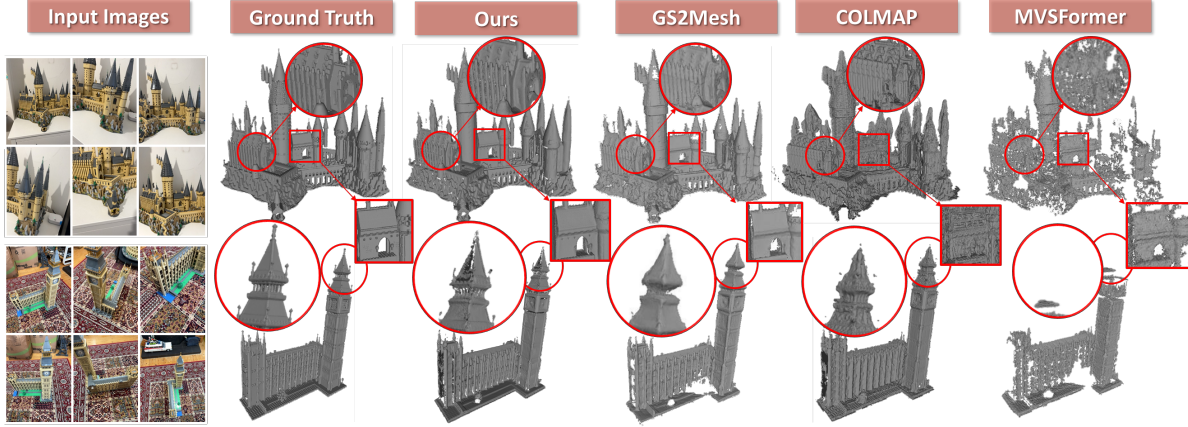


Figure 6. Mesh reconstruction comparison. With only multi-view RGB inputs, NeVStereo produces more accurate and geometrically faithful 3D reconstructions than competing methods.

Method	ScanNet++		Replica		NVIDIA-HOPE		WildUAV		
	absrel ↓	$\delta < 5\% \uparrow$	Acc $_{\pm 1\sigma}$ ↓ (m)						
DUSI3R [41]	0.0359	86.66%	0.0355	81.86%	0.0631	65.28%	0.0269	95.57%	0.311
MonST3R [48]	0.0348	86.77%	0.3653	13.29%	0.1381	36.51%	0.1251	42.59%	3.306
VGGT [39]	0.0312	84.47%	0.0096	98.05%	0.0409	80.67%	0.0403	83.64%	0.703
MapAnything [18]	0.0446	87.37%	0.0274	94.60%	0.0483	81.75%	0.0444	82.69%	0.779
π^3 [42]	0.0256	86.79%	0.0102	97.67%	0.0196	93.62%	0.0338	91.58%	0.556
Ours	0.0163	94.87%	0.0054	99.25%	0.0134	97.82%	0.0039	99.51%	0.058

Table 4. Multi-view depth estimation comparison across ScanNet++, Replica, NVIDIA-HOPE, and WildUAV. Our method achieves the best absrel and $\delta < 5\%$ accuracy on all datasets.

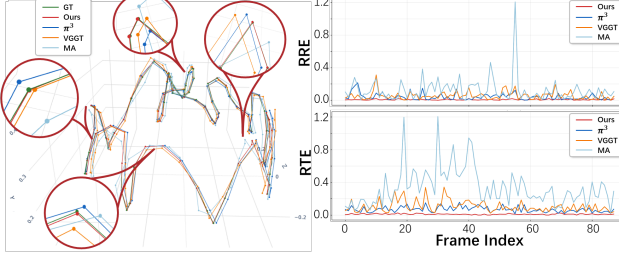


Figure 7. Trajectory and pose accuracy comparison. Left: estimated camera trajectory (red) nearly overlaps with the ground-truth trajectory (green). Right: per-frame RRE and RTE plots, where lower values indicate better pose accuracy.



Figure 8. Novel view synthesis comparison on ScanNet++. Our method produces sharper textures and more accurate geometry compared to baseline methods, including 3DGS and ZipNeRF.

6. Conclusion & Limitation

We presented NeVStereo, a NeRF-based NVS-stereo framework that jointly outputs high-accuracy pose, depth novel view synthesis, and 3D reconstruction at the same time. By combining multi-view confidence-guided optimization, depth-guided iterative refinement, and NeRF-coupled bundle adjustment, our method attains strong performance in camera pose estimation, depth estimation, novel view synthesis, and surface reconstruction on multiple datasets. Our study suggests that NeRF-based NVS-stereo can provide more stable, pose-robust reconstruc-

within Mv-CG shows a different trend: NeRF’s implicit geometry is less tied to SfM biases, and under Mv-CG constraints it better approximates the true scene depth, improving both pose accuracy and NeRF scores. Finally, adding the NeRF coupling loss yields the best overall performance—pose errors are further reduced while PSNR/SSIM improve and LPIPS decreases—indicating that joint optimization of geometry, pose, and rendering provides a more stable and mutually reinforcing solution.

Method	Input	Acc. (%) \uparrow		Rec. (%) \uparrow		F1 \uparrow		Chamfer (mm) \downarrow	
		$\sigma = 2.5$	$\sigma = 5$	$\sigma = 2.5$	$\sigma = 5$	$\sigma = 2.5$	$\sigma = 5$	(mm) \downarrow	
Neural-RGBD [1]	I+D	20.61	39.62	10.66	22.06	13.67	27.66	22.78	
COLMAP [31]	I+ P	74.89	93.79	68.20	84.53	71.08	88.71	5.26	
MVSFormer [6]	I+ P	80.77	96.33	55.02	71.32	64.60	81.14	9.11	
NeuS [40]	I+ P	77.35	93.33	70.85	86.11	73.74	89.30	4.74	
SurfaceSplat [10]	I	69.61	87.79	68.89	85.93	69.14	86.74	9.90	
GS2Mesh [45]	I	68.77	89.46	69.27	87.37	68.94	88.28	4.94	
Ours	I	82.60	97.86	71.49	86.67	76.64	91.93	4.35	

Table 5. Multi-view reconstruction experiment ($\sigma=2.5$ mm). Our method achieves the best overall accuracy, recall, F1, and Chamfer distance. Compared to neural-field-based approaches (e.g., NeuS, SurfaceSplat), MVS-based methods (e.g., COLMAP, MVSFormer) reconstruct accurately but can suffer from incomplete surface coverage. “I” denotes image input, “D” denotes requiring depth input, and “P” denotes requiring ground-truth camera poses.

Method	Pose			NeRF (Nerfacto)		
	ATE \downarrow	RTE \downarrow	RRE \downarrow	PSNR \uparrow	SSIM \uparrow	LPIPS \downarrow
COLMAP	1.85	0.97	0.067	24.51	0.85	0.203
DROID (w/o Mv-CG)	1.87	1.02	0.069	24.22	0.82	0.204
DROID (w/ Mv-CG)	1.84	0.95	0.066	24.31	0.83	0.201
DROID + GS depth	1.89	1.11	0.073	24.14	0.82	0.207
DROID-RGBD (Full)	1.75	0.93	0.065	25.54	0.84	0.195

Table 6. Ablation study on the Mobilebrick. Mv-CG denotes Multi-View Confidence-Guided Self-Supervised Optimization.

tions than 3DGS-based counterparts, with promising zero-shot generalization even on datasets used to train competing methods. Nonetheless, our pipeline still depends on COLMAP initialization and reliable NVS quality, and performance may deteriorate under extremely sparse views. Future work includes exploring self-supervised initialization and improved robustness to view sparsity.

References

- [1] Dejan Azinović, Ricardo Martin-Brualla, Dan B. Goldman, Matthias Nießner, and Justus Thies. Neural rgb-d surface reconstruction. In *Proceedings of the IEEE/CVF Conference on Computer Vision and Pattern Recognition (CVPR)*, page 6290–6301, 2022. [5](#), [9](#)
- [2] Jonathan T Barron, Ben Mildenhall, Dor Verbin, Pratul P Srinivasan, and Peter Hedman. Zip-nerf: Anti-aliased grid-based neural radiance fields. In *Proceedings of the IEEE/CVF International Conference on Computer Vision*, pages 19697–19705, 2023. [2](#), [6](#)
- [3] Siavash Arjomand Bigdeli, Gregor Budweiser, and Matthias Zwicker. Temporally coherent disparity maps using CRFs with fast high-dimensional filtering. In *Proceedings of the Asian Conference on Computer Vision (ACCV)*, 2014. [6](#)
- [4] Yohann Cabon, Lucas Stoffl, Leonid Antsfeld, Gabriela Csurka, Boris Chidlovskii, Jerome Revaud, and Vincent Leroy. Must3r: Multi-view network for stereo 3d reconstruction. In *Proceedings of the Computer Vision and Pattern Recognition Conference*, pages 1050–1060, 2025. [2](#)
- [5] Carlos Campos, Richard Elvira, Juan J Gómez Rodríguez, José MM Montiel, and Juan D Tardós. Orb-slam3: An accurate open-source library for visual, visual-inertial, and multimap slam. *IEEE transactions on robotics*, 37(6):1874–1890, 2021. [2](#)
- [6] Chenjie Cao, Xinlin Ren, and Yanwei Fu. Mvsformer: Multi-view stereo by learning robust image features and temperature-based depth. *arXiv preprint arXiv:2208.02541*, 2022. [9](#)
- [7] Pengcheng Chen, Wenhao Li, Nicole Gunderson, Jeremy Ruthberg, Randall Bly, Zhenglong Sun, Waleed M Abuzeid, and Eric J Seibel. Endoperfect: High-accuracy monocular depth estimation and 3d reconstruction for endoscopic surgery via nerf-stereo fusion. *arXiv preprint arXiv:2410.04041*, 2024. [2](#), [4](#), [6](#)
- [8] Valeria Croce, Dario Billi, Gabriella Caroti, Andrea Piemonte, Livio De Luca, and Philippe Véron. Comparative assessment of neural radiance fields and photogrammetry in digital heritage: impact of varying image conditions on 3d reconstruction. *Remote Sensing*, 16(2):301, 2024. [2](#)
- [9] Horațiu Florea, Vlad-Cristian Miclea, and Sergiu Nedevschi. Wilduav: Monocular uav dataset for depth estimation tasks. In *2021 IEEE 17th International Conference on Intelligent Computer Communication and Processing (ICCP)*, pages 291–298. IEEE, 2021. [7](#)
- [10] Zihui Gao, Jia-Wang Bian, Guosheng Lin, Hao Chen, and Chunhua Shen. Surfacesplat: Connecting surface reconstruction and gaussian splatting. In *Proceedings of the IEEE/CVF International Conference on Computer Vision*, pages 28525–28534, 2025. [9](#)
- [11] Antoine Guédon and Vincent Lepetit. Sugar: Surface-aligned gaussian splatting for efficient 3d mesh reconstruction and high-quality mesh rendering. In *Proceedings of the IEEE/CVF Conference on Computer Vision and Pattern Recognition*, pages 5354–5363, 2024. [2](#)
- [12] Jing Hu, Qinrui Fan, Shu Hu, Siwei Lyu, Xi Wu, and Xin Wang. Umednerf: Uncertainty-aware single view vol-

umetric rendering for medical neural radiance fields. In *2024 IEEE International Symposium on Biomedical Imaging (ISBI)*, pages 1–4. IEEE, 2024. 4

[13] Yue Hu, Rong Liu, Meida Chen, Peter Beerel, and Andrew Feng. Splatmap: Online dense monocular slam with 3d gaussian splatting. *Proceedings of the ACM on Computer Graphics and Interactive Techniques*, 8(1):1–18, 2025. 3

[14] Binbin Huang, Zehao Yu, Anpei Chen, Andreas Geiger, and Shenghua Gao. 2d gaussian splatting for geometrically accurate radiance fields. In *ACM SIGGRAPH 2024 conference papers*, pages 1–11, 2024. 2

[15] Hualie Jiang, Zhiqiang Lou, Laiyan Ding, Rui Xu, Minglang Tan, Wenjie Jiang, and Rui Huang. Defom-stereo: Depth foundation model based stereo matching. In *Proceedings of the Computer Vision and Pattern Recognition Conference*, pages 21857–21867, 2025. 2

[16] Junpeng Jing, Ye Mao, and Krystian Mikolajczyk. Match-stereo-videos: Bidirectional alignment for consistent dynamic stereo matching. In *European Conference on Computer Vision*, pages 415–432. Springer, 2024. 2

[17] Nikhil Keetha, Jay Karhade, Krishna Murthy Jatavallabhula, Gengshan Yang, Sebastian Scherer, Deva Ramanan, and Jonathon Luiten. Splatam: Splat track & map 3d gaussians for dense rgb-d slam. In *Proceedings of the IEEE/CVF Conference on Computer Vision and Pattern Recognition*, pages 21357–21366, 2024. 3

[18] Nikhil Keetha, Norman Müller, Johannes Schönberger, Lorenzo Porzi, Yuchen Zhang, Tobias Fischer, Arno Knapitsch, Duncan Zauss, Ethan Weber, Nelson Antunes, Jonathon Luiten, Manuel Lopez-Antequera, Samuel Rota Bulò, Christian Richardt, Deva Ramanan, Sebastian Scherer, and Peter Kortschieder. MapAnything: Universal feed-forward metric 3D reconstruction, 2025. *arXiv preprint arXiv:2509.13414*. 7, 8

[19] Bernhard Kerbl, Georgios Kopanas, Thomas Leimkühler, and George Drettakis. 3d gaussian splatting for real-time radiance field rendering. *ACM Trans. Graph.*, 42(4):139–1, 2023. 2

[20] Vincent Leroy, Yohann Cabon, and Jérôme Revaud. Grounding image matching in 3d with mast3r. In *European Conference on Computer Vision*, pages 71–91. Springer, 2024. 2

[21] Kejie Li, Jia-Wang Bian, Robert Castle, Philip HS Torr, and Victor Adrian Prisacariu. Mobilebrick: Building lego for 3d reconstruction on mobile devices. In *Proceedings of the IEEE/CVF Conference on Computer Vision and Pattern Recognition*, pages 4892–4901, 2023. 7

[22] Zhaoshuo Li, Thomas Müller, Alex Evans, Russell H Taylor, Mathias Unberath, Ming-Yu Liu, and Chen-Hsuan Lin. Neuralangelo: High-fidelity neural surface reconstruction. In *Proceedings of the IEEE/CVF Conference on Computer Vision and Pattern Recognition*, pages 8456–8465, 2023. 2

[23] Chen-Hsuan Lin, Wei-Chiu Ma, Antonio Torralba, and Simon Lucey. Barf: Bundle-adjusting neural radiance fields. In *Proceedings of the IEEE/CVF international conference on computer vision*, pages 5741–5751, 2021. 4

[24] Ben Mildenhall, Pratul P Srinivasan, Matthew Tancik, Jonathan T Barron, Ravi Ramamoorthi, and Ren Ng. Nerf. Representing scenes as neural radiance fields for view synthesis. *Communications of the ACM*, 65(1):99–106, 2021. 2

[25] Raul Mur-Artal, Jose Maria Martinez Montiel, and Juan D Tardos. Orb-slam: A versatile and accurate monocular slam system. *IEEE transactions on robotics*, 31(5):1147–1163, 2015. 2

[26] Jaesik Park, Qian-Yi Zhou, and Vladlen Koltun. Colored point cloud registration revisited. In *ICCV*, 2017. 3

[27] Keunhong Park, Philipp Henzler, Ben Mildenhall, Jonathan T Barron, and Ricardo Martin-Brualla. Camp: Camera preconditioning for neural radiance fields. *AcM Transactions on Graphics (TOG)*, 42(6):1–11, 2023. 4

[28] Anita Rau, Josiah Aklilu, F Christopher Holsinger, and Serena Yeung-Levy. Depth-guided nerf training via earth mover’s distance. In *European Conference on Computer Vision*, pages 1–17. Springer, 2024. 4

[29] Antoni Rosinol, John J Leonard, and Luca Carlone. Nerf-slam: Real-time dense monocular slam with neural radiance fields. In *2023 IEEE/RSJ International Conference on Intelligent Robots and Systems (IROS)*, pages 3437–3444. IEEE, 2023. 3, 5

[30] Sadra Safadoust, Fabio Tosi, Fatma Güney, and Matteo Poggi. Self-evolving depth-supervised 3d gaussian splatting from rendered stereo pairs. *arXiv preprint arXiv:2409.07456*, 2024. 2

[31] Johannes Lutz Schönberger and Jan-Michael Frahm. Structure-from-motion revisited. In *Conference on Computer Vision and Pattern Recognition (CVPR)*, 2016. 7, 9

[32] Thomas Schops, Torsten Sattler, and Marc Pollefeys. Bad slam: Bundle adjusted direct rgb-d slam. In *Proceedings of the IEEE/CVF Conference on Computer Vision and Pattern Recognition*, pages 134–144, 2019. 2

[33] Julian Straub, Thomas Whelan, Lingni Ma, Yufan Chen, Erik Wijmans, Simon Green, Jakob J Engel, Raul Mur-Artal, Carl Ren, Shobhit Verma, et al. The replica dataset: A digital replica of indoor spaces. *arXiv preprint arXiv:1906.05797*, 2019. 7

[34] Zachary Teed and Jia Deng. Droid-slam: Deep visual slam for monocular, stereo, and rgb-d cameras. *Advances in neural information processing systems*, 34:16558–16569, 2021. 2

[35] Adam Tonderski, Carl Lindström, Georg Hess, William Ljungbergh, Lennart Svensson, and Christoffer Petersson. Neurad: Neural rendering for autonomous driving. In *Proceedings of the IEEE/CVF Conference on Computer Vision and Pattern Recognition*, pages 14895–14904, 2024. 2

[36] Stephen Tyree, Jonathan Tremblay, Thang To, Jia Cheng, Terry Mosier, Jeffrey Smith, and Stan Birchfield. 6-dof pose estimation of household objects for robotic manipulation: An accessible dataset and benchmark. In *International Conference on Intelligent Robots and Systems (IROS)*, 2022. 3, 7

[37] Chen Wang, Jiadai Sun, Lina Liu, Chenming Wu, Zhelun Shen, Dayan Wu, Yuchao Dai, and Liangjun Zhang. Digging into depth priors for outdoor neural radiance fields. In *Proceedings of the 31st ACM International Conference on Multimedia*, pages 1221–1230, 2023. 4

[38] Jianyuan Wang, Nikita Karaev, Christian Rupprecht, and David Novotny. Vggsfm: Visual geometry grounded deep structure from motion. In *Proceedings of the IEEE/CVF conference on computer vision and pattern recognition*, pages 21686–21697, 2024. 7

[39] Jianyuan Wang, Minghao Chen, Nikita Karaev, Andrea Vedaldi, Christian Rupprecht, and David Novotny. Vggt: Visual geometry grounded transformer. In *Proceedings of the Computer Vision and Pattern Recognition Conference*, pages 5294–5306, 2025. 2, 7, 8

[40] Peng Wang, Lingjie Liu, Yuan Liu, Christian Theobalt, Taku Komura, and Wenping Wang. Neus: Learning neural implicit surfaces by volume rendering for multi-view reconstruction. *arXiv preprint arXiv:2106.10689*, 2021. 2, 9

[41] Shuzhe Wang, Vincent Leroy, Yohann Cabon, Boris Chidlovskii, and Jerome Revaud. Dust3r: Geometric 3d vision made easy. In *Proceedings of the IEEE/CVF Conference on Computer Vision and Pattern Recognition*, pages 20697–20709, 2024. 2, 7, 8

[42] Yifan Wang, Jianjun Zhou, Haoyi Zhu, Wenzheng Chang, Yang Zhou, Zizun Li, Junyi Chen, Jiangmiao Pang, Chunhua Shen, and Tong He. π^3 : Permutation-equivariant visual geometry learning. *arXiv preprint arXiv:2507.13347*, 2025. 2, 7, 8

[43] Frederik Warburg, Ethan Weber, Matthew Tancik, Aleksander Holynski, and Angjoo Kanazawa. Nerfbusters: Removing ghostly artifacts from casually captured nerfs. In *Proceedings of the IEEE/CVF International Conference on Computer Vision*, pages 18120–18130, 2023. 2

[44] Bowen Wen, Matthew Trepte, Joseph Aribido, Jan Kautz, Orazio Gallo, and Stan Birchfield. Foundationstereo: Zero-shot stereo matching. In *Proceedings of the Computer Vision and Pattern Recognition Conference*, pages 5249–5260, 2025. 2

[45] Yaniv Wolf, Amit Bracha, and Ron Kimmel. Gs2mesh: Surface reconstruction from gaussian splatting via novel stereo views. In *European Conference on Computer Vision*, pages 207–224. Springer, 2024. 2, 9

[46] Chi Yan, Delin Qu, Dan Xu, Bin Zhao, Zhigang Wang, Dong Wang, and Xuelong Li. Gs-slam: Dense visual slam with 3d gaussian splatting. In *Proceedings of the IEEE/CVF Conference on Computer Vision and Pattern Recognition*, pages 19595–19604, 2024. 3

[47] Chandan Yeshwanth, Yueh-Cheng Liu, Matthias Nießner, and Angela Dai. Scannet++: A high-fidelity dataset of 3d indoor scenes. In *Proceedings of the IEEE/CVF International Conference on Computer Vision*, pages 12–22, 2023. 7

[48] Junyi Zhang, Charles Herrmann, Junhwa Hur, Varun Jampani, Trevor Darrell, Forrester Cole, Deqing Sun, and Ming-Hsuan Yang. Monst3r: A simple approach for estimating geometry in the presence of motion. *arXiv preprint arXiv:2410.03825*, 2024. 7, 8

[49] Haoyin Zhou and Jayender Jagadeesan. Real-time dense reconstruction of tissue surface from stereo optical video. *IEEE transactions on medical imaging*, 39(2):400–412, 2019. 2

[50] Zihan Zhu, Songyou Peng, Viktor Larsson, Weiwei Xu, Hujun Bao, Zhaopeng Cui, Martin R. Oswald, and Marc Pollefeys. Nice-slam: Neural implicit scalable encoding for slam. In *Proceedings of the IEEE/CVF Conference on Computer Vision and Pattern Recognition (CVPR)*, pages 12786–12796, 2022. 5